Journal of Solid State Chemistry 182 (2009) 3305–3311

Contents lists available at ScienceDirect

Journal of Solid State Chemistry

journal homepage: www.elsevier.com/locate/jssc

Oxidation behaviour of uranium and neptunium in stabilised zirconia

Marcus Walter [a,*], Joseph Somers [a], Daniel Bouëxière [a], Piotr Gaczyński [a], Boris Brendebach [b]

[a] European Commission, Joint Research Centre, Institute for Transuranium Elements, P.O. Box 2340, D-76125 Karlsruhe, Germany
[b] Forschungszentrum Karlsruhe, Institut für Nukleare Entsorgung (INE), P.O. Box 3640, D-76021 Karlsruhe, Germany

ARTICLE INFO

Article history:
Received 20 July 2009
Received in revised form
15 September 2009
Accepted 16 September 2009
Available online 22 September 2009

Keywords:
Actinide
Transmutation
Nuclear waste disposal
Conditioning
Zirconia
Pyrochlore
EXAFS

ABSTRACT

Yttria stabilised zirconia (YSZ) based $(Zr,Y,U)O_{2-x}$ and $(Zr,Y,Np)O_{2-x}$ solid solutions with 6 and 20 mol% actinide were prepared with Y/Zr ratios ranging from 0.2 to 2.0 to investigate uranium and neptunium oxidation behaviour depending on the oxygen vacancies in the defect fluorite lattice. Sintering at 1600 °C in Ar/H_2 yields a cubic, fluorite-type structure with U(IV) and Np(IV). Annealing $(Zr,Y,U)O_{2-x}$ with Y/Zr=0.2 at 800 °C in air results in a tetragonal phase, whereas $(Zr,Y,U)O_{2-x}$ with higher Y/Zr ratios and $(Zr,Y,Np)O_{2-x}$ retain the cubic structure. XANES and O/*M* measurements indicate mixed U(V)–U(VI) and Np(IV)–Np(V) oxidation states after oxidation. Based on X-ray diffraction, O/*M* and EXAFS measurements, different oxidation mechanisms are identified for U- and Np-doped stabilised zirconia. In contrast to U, excess oxygen vacancies are needed to oxidise Np in $(Zr,Y,Np)O_{2-x}$ as the oxidation process competes with Zr for oxygen vacancies. As a consequence, U(VI) and Np(V) can only be obtained in stabilised zirconia with Y/Zr=1 but not in YSZ with Y/Zr=0.2.

1. Introduction

Stabilised zirconia finds wide applications due to its ion conductivity and oxygen storage capacity. It is also considered as a host matrix for plutonium and minor actinides (*MA*=Np, Am, Cm), either for their transmutation in dedicated reactor systems [1,2] or to condition these long-lived actinides in a radiation-resistant, durable form for final disposal [3,4]. Zirconia, ZrO_2, is monoclinic, but can be stabilised in tetragonal and cubic forms by addition of large trivalent dopant atoms, such as the rare earth elements. Cubic stabilised zirconia crystallises in a defect fluorite structure ($Fm\bar{3}m$), where the metal atoms are randomly distributed. Ordered $A_2Zr_2O_7$ ($Fd\bar{3}m$, pyrochlore) and $B_4Zr_3O_{12}$ ($R\bar{3}$) structures are formed in the case of larger (*A*=La–Gd) and smaller rare earth elements (*B*=Sc, Y, Ho–Lu), respectively. For nuclear fuel or waste applications the most favoured matrices are cubic yttria stabilised zirconia, YSZ: $(Zr_{0.84}Y_{0.16})O_{1.92}$, and pyrochlores like $Nd_2Zr_2O_7$ or $Gd_2Zr_2O_7$.

The incorporation of tetravalent actinides in YSZ can easily be achieved as their dioxides are isostructural with cubic YSZ. Trivalent Pu, Am, and Cm have ionic radii similar to the large rare earth elements and can either stabilise cubic zirconia or form an ordered pyrochlore structure if the stoichiometry comes close to $A_2Zr_2O_7$. As the valence of the actinide elements depends strongly on the oxygen potential during processing, different oxidation states can be obtained by applying reducing or oxidising conditions, at moderate or high temperature. Once incorporated in a stabilised zirconia matrix, Pu and Am are tetravalent when oxidised at moderate temperatures or trivalent when reduced at high temperatures in Ar/H_2 [5–9]. In contrast, for neptunium and uranium, the lowest oxidation state in stabilised zirconia is Np(IV) and U(IV) [6,10–12]. Mössbauer spectra of ^{237}Np in YSZ with 14 mol% Y have indicated the predominance of Np(IV) and a minor contribution from Np(V) [6]. In the cubic $(Nd_{1.8}Np_{0.2})Zr_2O_{7+x}$ pyrochlore compound, Np(IV) and Np(V) were found when the material was first treated in Ar/H_2 and then annealed in air [9]. The formation of Np(V) is facilitated if oxygen vacancies are present in the solid solution. UO_2 forms a solid solution with Ca stabilised zirconia and zirconolite, $CaZrTi_2O_7$, and the formation of a mixed U(IV–V) oxidation state has been observed on oxidation [11–14]. However, the influence of the vacancy concentration linked to the Y content, on the relative Np and U oxidation states in stabilised zirconia, has not been studied in a systematic way.

The local atomic structure in the YSZ solid solution has been investigated by extended X-ray absorption fine structure (EXAFS) and a different coordination environment was found for Y and Zr atoms. According to these EXAFS results, the oxygen vacancies created by the trivalent Y(III) dopant ion are mainly associated with the Zr atoms [15–17], which has been confirmed using ^{89}Y MAS–NMR [18]. Finally, EXAFS has been used to identify the local actinide structure in zirconia-based materials with defect fluorite structure [8,19].

* Corresponding author. Fax: +49 7247 951 566.
E-mail addresses: 1052076@web.de (M. Walter), joseph.somers@ec.europa.eu (J. Somers).

0022-4596/$ - see front matter © 2009 Published by Elsevier Inc.
doi:10.1016/j.jssc.2009.09.022

The aim of the present study is a systematic investigation on the oxidation behaviour of uranium and neptunium incorporated in stabilised zirconia, and its dependence on the yttrium content in YSZ. The knowledge of possible or limiting actinide oxidation states inside the stabilised zirconia is mandatory for the assessment of such matrices as either fuels or conditioning matrices. The local structure within the solid solutions and their impact on the actinide oxidation have been studied using X-ray absorption spectroscopy.

2. Experimental

2.1. Sample preparation

$(Zr,Y,U)O_{2-x}$ samples were prepared by gel-supported precipitation [1,20]. Briefly, Zr–Y stock solutions were prepared with Y/Zr ratios of 0.2 (Y/Zr+Y=0.16), 0.5 (Y/Zr+Y=0.33), 1 (Y/Zr+Y=0.50), and 2 (Y/Zr+Y=0.67) using zirconyl chloride and yttrium nitrate (both Alfa Aesar 99.9%) as starting materials. Uranyl nitrate solution was added to obtain a stoichiometry of U/(Zr+Y+U) of 0.06, 0.12, 0.20, 0.50, 0.75. The viscosity was adjusted by addition of an organic thickener (Methocel, Dow Chemicals) and this solution was then dropped in an ammonia bath where droplet to particle conversion took place due to hydrolysis of the metal ions. The resulting beads were washed, dried in propanol, and calcined at 800 °C in air (2 h) to remove organics and then subsequently under Ar/H_2 (6% H_2) to obtain U(IV). Pellets were pressed and sintered at 1600 °C under Ar/H_2 (12 h).

As the $(Zr,Y,Np)O_{2-x}$ samples were prepared at a smaller scale, powder metallurgy was used instead of the gel-supported precipitation route. Therefore, part of Zr–Y solution used for the U samples was precipitated, calcined at 600 °C and milled. The $(Zr,Y)O_{2-x}$ powders were then carefully milled with NpO_2 powder to obtain $(Zr,Y,Np)O_{2-x}$ samples with Np/Zr+Y+Np ratios of 0.06, 0.20, and 0.50. Pellets were pressed and sintered at 1600 °C under Ar/H_2 (24 h), milled, pressed again, and resintered under the same conditions.

Additional samples were needed for the EXAFS analysis, as the Y *K*-edge (17038 eV) and the U L_3-edge (17168 eV) are too close to derive meaningful EXAFS spectra for $(Zr,Y,U)O_{2-x}$. Lutetium was chosen as replacement for Y as it is invariably trivalent and no pyrochlore is formed at $(Zr_{0.5}Lu_{0.5})O_{1.75}$ as the Lu ionic radius is too small. The $(Zr,Lu,U)O_{2-x}$ samples were prepared with the same stochiometry and preparation route as the $(Zr,Y,Np)O_{2-x}$ samples. UO_2, U_3O_8, and $BaUO_4$ [21] were used as X-ray absorption near edge spectroscopy (XANES) reference compounds.

2.2. Sample analysis

The O/U and O/Np ratios in the U and Np containing zirconia compounds were determined by the weight change observed when treated at 800 °C in air (24 h, 50 K/h cool down) and Ar/H_2 (24 h, 200 K/h cool down). The latter is a usual reference treatment establishing U(IV) and Np(IV). For the $(Zr,Y,Np)O_{2-x}$ samples reduction at 800 °C was found sufficient to reach Np(IV). However, the $(Zr,Y,U)O_{2-x}$ samples reduced in Ar/H_2 at 800 °C and 1600 °C revealed a systematic difference of O/U with increasing Y content, which can be attributed to a change in the $(Zr,Y,U)O_{2-x}$ oxidation potential. Consequently the masses obtained by reductive treatment at 1600 °C were used for O/U determination.

Powder X-ray diffraction patterns were obtained for both reduced and oxidised samples using a Bruker D8 diffractometer ($CuK\alpha_1$, Ge monochromator) equipped with a position-sensitive detector (Vantec). Measurements were performed from 20° to 120° 2θ with incremental steps of 0.0085°. The lattice parameter was refined using the Fullprof suite [22]. The ^{237}Np Mössbauer measurement on an oxidised $(Zr_{0.4}Y_{0.4}Np_{0.2})O_{1.85}$ sample was performed at 4 K with a conventional transmission geometry spectrometer. The isomer shift, IS, is given relative to $NpAl_2$ at 4 K.

X-ray absorption spectra at the Zr, Y *K*-edge, and Lu, U and Np L_3-edge were recorded in transmission mode at the INE-Beamline [23] at the Ångströmquelle Karlsruhe, ANKA. A pair of Ge(4 4 2) crystals (Si(1 1 1) in case of Lu L_3-edge) was used in the double crystal monochromator. Two Rh-coated mirrors ensured the rejection of higher harmonics at this beamline. The EXAFS oscillations were extracted according to standard procedures using WINXAS [24]. The threshold energy, E_0, was defined as the first maximum of the first derivate of the XANES region. Spherical 8 Å clusters of atoms with the Cartesian coordinates of $(Zr,Lu,U)O_2$ and $(Zr,Y,Np)O_2$ were used for the calculation of the theoretical phase shifts, $\delta(k)$, and backscattering amplitude functions, $F(k)$, (FEFF8 [25]). The amplitude reduction factor was held constant at 1.0 for the EXAFS fits and the shift in threshold energy, ΔE_0, was varied as a global parameter. The EXAFS data were refined in *R*-space (1–4 Å) from the Fourier-transformed k^3-weighted $\chi(k)$ data. The *k*-range was limited by element absorption edges at next higher energies (i.e. 2.6–11.2 $Å^{-1}$ for Zr, 2.5–10.7 $Å^{-1}$ for Y, 2.9–8.8 $Å^{-1}$ for Lu, 3.1–9.4 $Å^{-1}$ for Np, and 3.2–10 $Å^{-1}$ for U, depending on spectra quality).

3. Results

3.1. X-ray diffraction

The X-ray diffraction patterns of $(Zr,Y,U)O_{2-x}$ and $(Zr,Y,Np)O_{2-x}$ sintered at 1600 °C in Ar/H_2 revealed the formation of a single fluorite-type ($Fm\bar{3}m$) solid solution within the investigated stoichiometry ranges. The lattice parameter (Fig. 1) increases with the Y, U, and Np contents.

Under oxidising conditions (800 °C, air) the cubic fluorite structure of $(Zr,Y,U)O_{2-x}$ is less stable. At low Y contents and relatively high uranium ratios U/(Zr+Y+U) of 0.5 and 0.75, the $(Zr,Y,U)O_{2-x}$ solid solutions decompose to ZrU_2O_7 [26] and U_3O_8. This instability can be suppressed by increasing the Y content and the fluorite structure of $(Zr_{0.17}Y_{0.33}U_{0.5})O_{1.84}$ remains stable during oxidation. A second transformation is observed for $(Zr,Y,U)O_{2-x}$ samples at a Y/Zr ratio of 0.2, i.e. $(Zr_{0.84}Y_{0.16})O_{1.92}$ mixed with 6, 12, and 20 mol% UO_2. Here the structure of the solid solution changed from cubic ($Fm\bar{3}m$) to a tetragonal subgroup ($P4_2/nmc$) on oxidation. This is essentially the same distorted fluorite structure that forms in pure YSZ with even lower Y content [27]. Obviously, the yttrium content in these samples is too small to compensate for the destabilising force of the oxidised uranium atoms. All other samples with Y/Zr of 0.5, 1, 2 and U/(Zr+Y+U) ratios of 0.06, 0.12, and 0.20 maintain in the fluorite structure during oxidation. Their lattice parameter is always smaller than for the reduced sample (Fig. 1). When Y is replaced by Lu, i.e. for the $(Zr,Lu,U)O_{2-x}$ samples for EXAFS spectroscopy, the same phase relationship was found as for $(Zr,Y,U)O_{2-x}$. The lattice parameter of the $(Zr,Lu,U)O_{2-x}$ solid solutions is always smaller, as can be expected from the ionic radii (Y 1.02 Å, Lu 0.98 Å). For the $(Zr,Y,Np)O_{2-x}$ samples no transformation into tetragonal symmetry was observed and all samples maintain the cubic fluorite structure during oxidation. Most notably, the change in lattice parameter upon oxidation is much smaller compared to $(Zr,Y,U)O_{2-x}$ and is nearly zero for $(Zr,Y,Np)O_{2-x}$ with Y/Zr=0.2.

3.2. O/M determination

The oxygen to metal (O/*M*) ratio was measured for solid solutions maintaining the fluorite structure ($Fm\bar{3}m$ and $P4_2/nmc$)

during oxidation. The data are shown in Figs. 2 and 3 (left) as a function of the actinide content in $(Zr,Y,U)O_{2-x}$ and $(Zr,Y,Np)O_{2-x}$, respectively. Generally, the O/*M* of the oxidised samples decreases as the actinide content in the solid solution increases. The O/*M* increases with the Y/Zr ratio, i.e. with the amount of oxygen vacancies. To resolve these effects, a data reduction method is deployed and the O/*M* is plotted versus different stoichiometric ratios (Figs. 2 and 3, right).

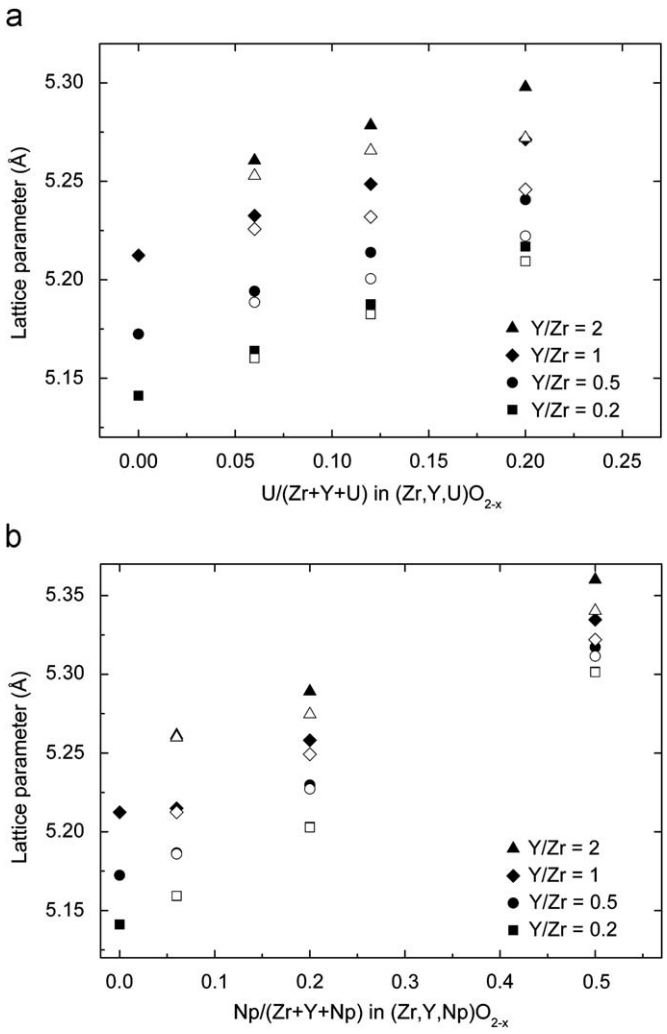

Fig. 1. Lattice parameter of $(Zr,Y,U)O_{2-x}$ and $(Zr,Y,Np)O_{2-x}$ sintered at 1600 °C under Ar/H_2 (closed) and oxidised at 800 °C in air (open). A pseudocubic unit cell $a' = \sqrt[3]{2a^2c}$ [27] is given instead the tetragonal parameters for oxidised $(Zr,Y,U)O_{2-x}$ with Y/Zr=0.2.

The O/U ratio of oxidised $(Zr,Y,U)O_{2-x}$ clearly depends on the Y/U ratio of the compound (Fig. 2, right). The O/U ratio is not lower than 2.5 (Y/U=0.8), and increases with Y/U in an intermediate range and remains close to 3.0 without further increase at high Y/U ratios. Obviously $(Zr,Y,U)O_{2-x}$ oxidises significantly even when the number of oxygen vacancies is low. This agrees with the general tendency of pure UO_2 to accommodate excess oxygen atoms in its lattice. At intermediate Y/U ratios the amount of oxidised uranium (O_2 uptake) depends on the amount of oxygen vacancies caused by the trivalent yttrium ions until nearly all uranium reach U(VI). A significant colour change of the oxidised samples was observed, ranging from black ($O/U < 2.8$) via brown to orange ($O/U > 2.9$), whereas the colour of the reduced samples is greenish grey.

The same data reduction was applied to the O/Np data, but was not conclusive. Instead another dependency was found for the $(Zr,Y,Np)O_{2-x}$ samples. Here, O/Np correlates linearly with the Y/(Zr+Np) ratio of the solid solutions (Fig. 3, right), which indicates that the degree of Np oxidation is influenced by the amount of Zr and Np. This can also be seen in the O/Np versus Np/(Zr+Y+Np) plot (Fig. 3, left), where a dramatic increase of Np oxidation occurs with increase in Y/Zr ratio. It appears that the oxidation susceptibility of Np is low, so that Np has to compete with Zr for oxygen vacancies (see below for discussion). For most of the oxidised samples a mixed Np(IV)–Np(V) valence can be assumed. However, an Np/O ratio of 2.63 suggests the presence of Np(VI) in the sample with highest Y(Zr+Np) ratio. The colour of the reduced samples was grey, with only minor changes during oxidation.

3.3. XANES

X-ray absorption near edge spectra (XANES) of $(Zr,Lu,U)O_{2-x}$ and $(Zr,Y,Np)O_{2-x}$ were recorded at the U and Np L_3-edges. Representative XANES spectra of reduced and oxidised samples with 6 mol% actinide and Lu/Zr (Y/Zr) ratios of 0.2 and 1 are shown in Fig. 4. The U and Np L_3-edge position, defined as the position of the white line, of the reduced samples is at the same energy, independent of the Lu/Zr and Y/Zr ratio. Furthermore, the energy position coincidences with those of pure UO_2 and NpO_2 (not shown for clarity reason), confirming the formation of U(IV) and Np(IV) under reducing conditions. The edge positions shift to higher energies upon

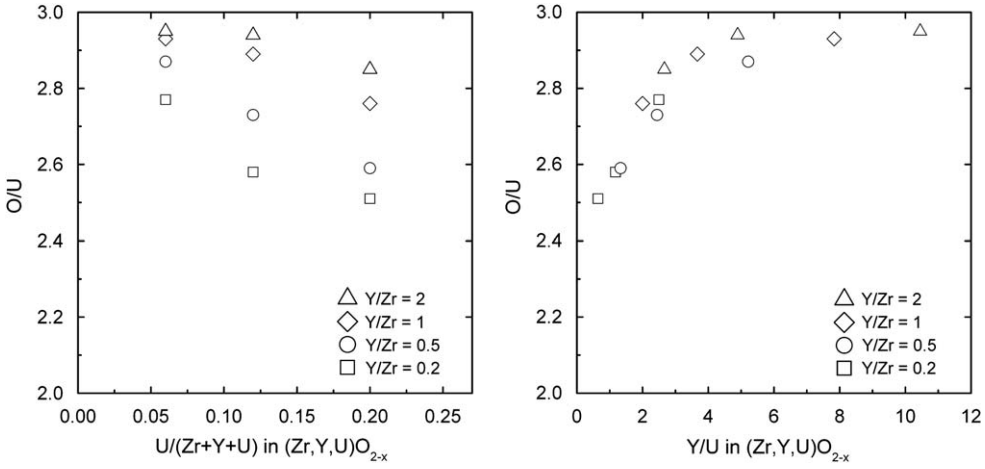

Fig. 2. (Left) O/U versus the U content in $(Zr,Y,U)O_{2-x}$. (Right) The measured O/U ratio shows a clear dependence on the Y/U ratio, i.e. the degree of uranium oxidation depends on the amount of oxygen vacancies.

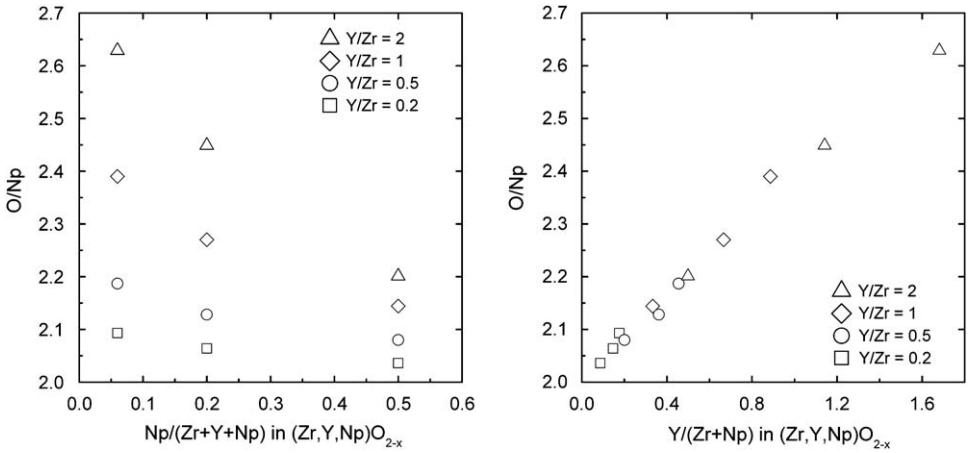

Fig. 3. (Left) O/Np versus the Np content in $(Zr,Y,Np)O_{2-x}$. (Right) The correlation of O/Np and Y/(Zr+Np) indicates that both Zr and Np compete for oxygen vacancies, which hinders the Np oxidation at low Y/Zr ratios.

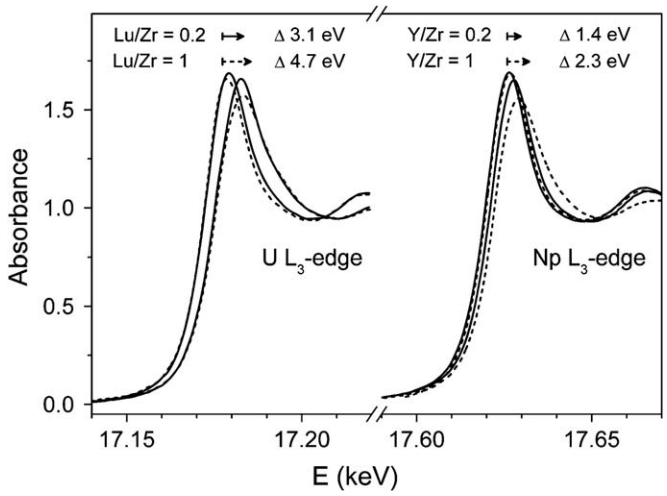

Fig. 4. Normalised L_3-edge XANES spectra of U and Np in $(Zr,Lu,U)O_{2-x}$ and $(Zr,Y,Np)O_{2-x}$ containing 6 mol% actinide. The energy position of the reduced samples corresponds well with UO_2 and NpO_2. The spectra of the oxidised samples are shifted to higher energies depending on the oxygen vacancy concentration indicated by the Lu/Zr and Y/Zr ratios (solid Lu/Zr and Y/Zr=0.2, dash Lu/Zr and Y/Zr=1).

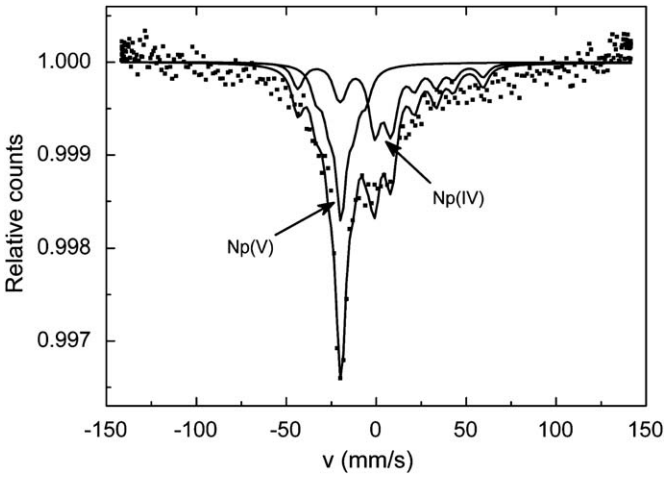

Fig. 5. ^{237}Np Mössbauer spectrum of the oxidised $(Zr_{0.4}Y_{0.4}Np_{0.2})O_{1.85}$ sample recorded at 4 K.

oxidation, and the shift increases in magnitude with the Lu/Zr and Y/Zr ratio, respectively. The shift is larger for uranium than for neptunium and therefore the U valance after oxidation is higher than that for Np. For the oxidised 6 mol% uranium samples the U L_3-edge position is between those of U_3O_8 and $BaUO_4$. This confirms the results from the O/*M* determination.

Neptunium and uranium in the (V) and (VI) oxidation states often form oxocations, e.g. uranyl and neptunyl groups, with two oxygen atoms at a short distance of approximately 1.8 Å. The L_3-edge position of such species is then close to those of the (IV) cations [28] and the XANES reveals a multiple scattering (MS) feature approximately 15 eV above the edge [29]. The absence of the MS feature in these data and the edge shift to higher energies exclude the formation of such a structural unit in the oxidised samples in this work. Similar observations were made for U and Np incorporated in a $Nd_2Zr_2O_7$ pyrochlore [9], where no evidence for oxocations was found either.

3.4. ^{237}Np Mössbauer spectroscopy

An ^{237}Np Mössbauer spectrum was recorded for the oxidised $(Zr_{0.4}Y_{0.4}Np_{0.2})O_{1.85}$ sample at 4 K (Fig. 5). The spectrum reveals two Np species with isomer shifts of −10 and −33 mm/s, which were assigned to Np(IV) and Np(V), respectively. The peak deconvolution indicates the presence of 50% Np(V) by area. This corresponds quite well with the measured O/Np ratio of 2.27 (Fig. 3).

3.5. EXAFS

Representative k^3-weighted Zr, Y, Lu, U, and Np EXAFS data and their corresponding Fourier transforms (FT) are shown in Fig. 6 for $(Zr,Lu,U)O_{2-x}$ and $(Zr,Y,Np)O_{2-x}$ samples with 6 mol% actinide content. The FTs reveal two peaks corresponding to the first coordination shell of 7–8 oxygen atoms and a second coordination shell of 12 metal atoms, which are either Zr+Lu+U or Zr+Y+Np. When comparing the FT peak intensities, the different *k*-range used for the evaluation of the EXAFS data (due to element absorption edges at next higher energies) should be noted. However, the second peak intensities are much lower for the Lu/Zr=1 samples compared to those with Lu/Zr=0.2. This is due to the destructive interference of the individual metal–metal scattering paths, e.g. the Zr–Zr and Zr–Lu paths have different backscattering phase shifts and partly cancel each other out.

The experimental EXAFS data were fitted in *R*-space using a two-shell model consisting of 7–8 oxygen and 12 metal atoms. For simplicity Zr alone was chosen for samples where Zr or Zr+Y is the

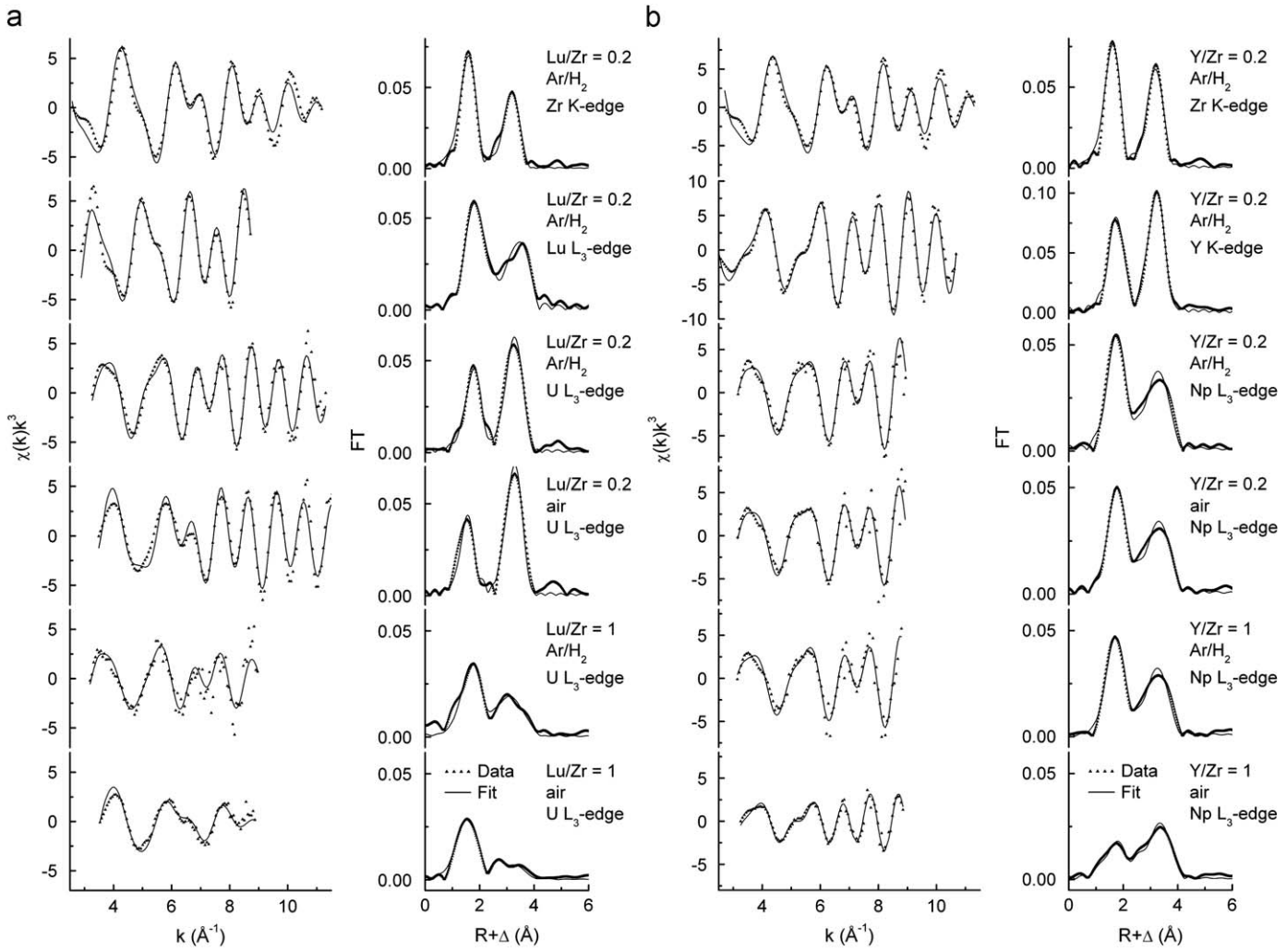

Fig. 6. Representative Zr, Y *K*-edge, Lu, U, Np L_3-edge EXAFS spectra of (left) $(Zr,Lu,U)O_{2-x}$ and (right) $(Zr,Y,Np)O_{2-x}$ containing 6 mol% actinide.

dominating metal atom according to stoichiometry. Taking the different backscattering behaviour of Zr, Lu, U, and Np into consideration, a three-shell model was applied for samples with 20 mol% actinide content and samples with Lu/Zr=1. The Debye–Waller factor σ^2 for the two metal shells was correlated during the fit. Fits including all three metal atoms according to stoichiometry (e.g. a four-shell model) were tested, but three metal–metal distances are too close to each other to derive meaningful structural parameters. The coordination number *N* of the oxygen atoms was set to 8 for samples with Lu/Zr and Y/Zr=0.2. In case of the Lu/Zr and Y/Zr=1 samples *N* was set to 7, or higher, to account for the increase in oxygen vacancies. For the oxidised $(Zr,Lu,U)O_{2-x}$ samples with tetragonal symmetry a split oxygen shell each with 4 O atoms was assumed, as it corresponds to their crystallographic structure [27]. The obtained structural parameters of the first coordination shell are listed in Tables 1 and 2. The complete set of structural parameters is provided as Supplementary data.

The EXAFS data analysis indicates element-specific metal–oxygen bond lengths in the investigated solid solutions treated under Ar/H_2. In reduced solid solutions with a low number of oxygen vacancies (Lu/Zr and Y/Zr=0.2) the bond lengths are as follows: Zr–O 2.14–2.15 Å, Y–O 2.31 Å, Lu–O 2.27 Å, U(IV)–O 2.28–2.29 Å, and Np(IV)–O 2.27–2.28 Å. In the corresponding solid solutions with a higher number of oxygen vacancies (Lu/Zr and Y/Zr=1) the bond lengths are about 0.02 Å shorter. Although the

Table 1
Metal–oxygen bond lengths in $(Zr,Lu,U)O_{2-x}$.

	N[a]	R (Å)[b]	σ^2 (Å^2)[c]	N	R (Å)	σ^2 (Å^2)
	$(Zr_{0.79}Lu_{0.15}U(IV)_{0.06})O_{1.92}$			$(Zr_{0.79}Lu_{0.19}U(ox)_{0.06})O_{1.97}$		
Zr–O	8	2.14	0.0124	4	2.11	0.0066
Zr–O				4	2.27	0.0287
Lu–O	8	2.27	0.0121	4	2.21	0.0021
Lu–O				4	2.39	0.0046
U–O	8	2.28	0.0121	4	2.08	0.0061
U–O				4	2.25	0.0100
	$(Zr_{0.67}Lu_{0.13}U(IV)_{0.20})O_{1.94}$			$(Zr_{0.67}Lu_{0.13}U(ox)_{0.20})O_{2.04}$		
Zr–O	8	2.14	0.0116	4	2.11	0.0067
Zr–O				4	2.30	0.0253
Lu–O	8	2.27	0.0119	4	2.22	0.0041
Lu–O				4	2.40	0.0099
U–O	8	2.29	0.0096	4	2.15	0.0096
U–O				4	2.25	0.0211
	$(Zr_{0.47}Lu_{0.47}U(IV)_{0.06})O_{1.77}$			$(Zr_{0.47}Lu_{0.47}U(ox)_{0.06})O_{1.82}$		
Zr–O	7	2.12	0.0088	7	2.13	0.0087
Lu–O	7	2.24	0.0127	7	2.25	0.0124
U–O	7	2.25	0.0141	7	2.12	0.0171
	$(Zr_{0.40}Lu_{0.40}U(IV)_{0.20})O_{1.80}$			$(Zr_{0.40}Lu_{0.40}U(ox)_{0.20})O_{1.95}$		
Zr–O	7.2	2.13	0.0084	7.8	2.15	0.0103
Lu–O	7.2	2.25	0.0121	7.8	2.27	0.0126
U–O	7.2	2.27	0.0130	7.8	2.16	0.0146

[a] *N*, coordination number.
[b] *R*, interatomic distance.
[c] σ^2, Debye–Waller factor.

Table 2
Metal–oxygen bond lengths in $(Zr,Y,Np)O_{2-x}$.

	N[a]	R (Å)[b]	σ^2 (Å^2)[c]	N	R (Å)	σ^2 (Å^2)
	$(Zr_{0.79}Y_{0.15}Np(IV)_{0.06})O_{1.92}$			$(Zr_{0.79}Y_{0.19}Np(ox)_{0.06})O_{1.93}$		
Zr–O	8	2.14	0.0117	8	2.14	0.0111
Y–O	8	2.31	0.0090	8	2.31	0.0088
Np–O	8	2.27	0.0092	8	2.29	0.0106
	$(Zr_{0.67}Y_{0.13}Np(IV)_{0.20})O_{1.94}$			$(Zr_{0.67}Y_{0.13}Np(ox)_{0.20})O_{1.95}$		
Zr–O	8	2.15	0.0111	8	2.14	0.0114
Y–O	8	2.31	0.0087	8	2.30	0.0079
Np–O	8	2.28	0.0086	8	2.28	0.0092
	$(Zr_{0.47}Y_{0.47}Np(IV)_{0.06})O_{1.77}$			$(Zr_{0.47}Y_{0.47}Np(ox)_{0.06})O_{1.79}$		
Zr–O	7	2.13	0.0084	7	2.13	0.0082
Y–O	7	2.30	0.0103	7	2.30	0.0100
Np–O	7	2.25	0.0093	7	2.25	0.0249
	$(Zr_{0.40}Y_{0.40}Np(IV)_{0.20})O_{1.80}$			$(Zr_{0.40}Y_{0.40}Np(ox)_{0.20})O_{1.85}$		
Zr–O	7.2	2.13	0.0079	7.2	2.14	0.0079
Y–O	7.2	2.29	0.0094	7.2	2.30	0.0094
Np–O	7.2	2.25	0.0094	7.2	2.27	0.0187

[a] N, coordination number.
[b] R, interatomic distance.
[c] σ^2, Debye–Waller factor.

error in determining interatomic distances is approximately 0.01 Å, the systematic shortening of the bond lengths can be attributed to the lower coordination number caused by the increase in oxygen vacancy concentration.

The structural changes induced by oxidation in air are different for U- and Np-doped samples and indeed for the Lu/Zr and Y/Zr ratio of the solid solutions. The oxidised $(Zr,Lu,U)O_{2-x}$ solid solutions with Lu/Zr=0.2 are tetragonal and a split oxygen shell with characteristic bond length values surrounds Zr, Lu, and U atoms. Especially for U–O, the bond lengths increase with the uranium content and the associated lower O/U ratio. Oxidised $(Zr,Lu,U)O_{2-x}$ solid solutions with Lu/Zr=1 are cubic and a single U–O distance is found at 2.12 Å (6 mol% U, O/U=2.93) and 2.16 Å (20 mol% U, O/U=2.76). The Zr–O and Lu–O bond distances of these two oxidised samples are slightly larger than the reduced solid solutions. This can be attributed to a change in the oxygen coordination number as vacancies are filled upon oxidation. In case of the $(Zr,Y,Np)O_{2-x}$ solid solutions the effect of oxidation on the local structure is less dramatic, as the oxidation of Np is much lower compared to U. The bond lengths in the $(Zr,Y,Np)O_{2-x}$ solid solutions with Y/Zr=0.2 are essentially the same as for the reduced samples, which agrees with the O/Np close to 2.0 for these samples. A remarkable change in the EXAFS spectra and FTs can be noticed for the oxidised $(Zr,Y,Np)O_{2-x}$ solid solutions with Y/Zr=1, but the determined M–O bond length is similar in both reduced and oxidised samples. However, the disorder (σ^2) is much higher, indicating a static distorted oxygen shell surrounding Np. Possibly, the low k-range of the spectra (due to the Zr K-edge at 17998 eV) prevents the detection of a shorter Np–O bond length in those mixed Np(IV)–Np(V) samples.

4. Discussion and conclusion

4.1. Local structure impact on U and Np oxidation

Element-specific bond lengths typical for cubic stabilised zirconia were observed by EXAFS spectroscopy. The observed U(IV)–O (2.28–2.29 Å) and Np(IV)–O (2.27–2.28 Å) bond distances are similar to those reported for Ce(IV)–O (2.24–2.25 Å [30]) and Am(IV)–O (2.27–2.29 Å [8]) incorporated in yttria stabilised zirconia with Y/Zr=0.2. The Nd(III)–O (2.40–2.42 Å [30]) and Am(III)–O (2.37 Å [8]) bond lengths are significantly higher. The shortening of all the (Zr,Y,Lu,U,Np)–O bonds at Y/Zr and Lu/Zr=1 clearly reveals that all metals accept oxygen vacancies. However, ^{89}Y MAS–NMR measurements of YSZ indicate that even at Y/Zr=1, Zr is surrounded by less oxygen atoms than Y [18]. This is in agreement with the general accepted stabilisation mechanism, where the preferential acceptance of oxygen vacancies by Zr is seen as the driving force of the tetragonal and cubic phase stabilisations in $(Zr,Y)O_{2-x}$ [15–17]. The incorporation of actinides in stabilised zirconia can modify the number of oxygen vacancies in the solid solution. When trivalent actinides like in $(Zr,Y,Am)O_{2-x}$ with Y/Zr=0.2 are incorporated, more oxygen vacancies are created, which mainly lowers the number of oxygen atoms surrounding the Zr atoms. Upon Am(III) oxidation to Am(IV) these vacancies are filled and an expansion of the Zr–O and Zr–M distances together with Am–O contraction is found in EXAFS studies [8].

Table 3
Oxidation state of actinides in stabilised zirconia.

Th	Pa	U	Np	Pu	Am	Cm
				3[a]	3[a]	3
4	4[a,b]	4[a]	4[a]	4[c]	4[c]	4[b,d]
	5[b,c]	5[c]	5[d]			
		6[d]				

[a] Reducing conditions (e.g. Ar/H_2 at high temperature).
[b] Proposed.
[c] Oxidative conditions (e.g. air at moderate temperature).
[d] Oxidative conditions and oxygen vacancies.

The incorporation of 6–20 mol% U(IV) and Np(IV) into stabilised zirconia will not directly affect the number of oxygen vacancies. However, the oxidation of U and Np depends on the available oxygen vacancy concentration. UO_2 is known to accept interstitial oxygen atoms in the fluorite lattice up to $UO_{2.25}$. Once incorporated in YSZ uranium can be oxidised to a mixed U(V)–U(VI) valence at Y/Zr=0.2, but the elimination of oxygen vacancies associated with Zr atoms destabilises the cubic phase and a tetragonal phase is formed. In solid solutions with excess oxygen vacancies, e.g. Y/Zr=1, the formation of U(VI) is possible without destabilising the cubic phase as enough oxygen vacancies will remain to keep the Zr–O coordination number lower than eight. The oxidation susceptibility of Np is much lower than U, and the Np(IV) oxidation process has to compete with the affinity of oxygen vacancies to the Zr atoms. Consequently, Np oxidation is suppressed at Y/Zr=0.2. A substantial increase of O/Np is found for high Y/Zr (Fig. 3) as sufficient vacancies are present to keep the Zr–O coordination number below eight while simultaneously Np can be oxidised to Np(V) or higher.

4.2. Oxidation state of actinides in stabilised zirconia

The knowledge of the actinide oxidation state in the stabilised zirconia matrix is of fundamental importance as the material will undergo several chemical transformations during its nuclear application. Transmutation (e.g. fission, decay) produces significant amounts of metallic or lower charged elements, which increases the oxygen potential (pO_2) in the irradiated fuel. Conditioning of Pu and *MA* results in decay products, and potentially easily leachable actinide species like U(VI) or Np(V) could be formed through a contact with ground water during long-term storage. The possible oxidation states in stabilised zirconia are summarised in Table 3 for actinides with nuclear and environmental relevance.

Generally the lower actinide oxidation state can be obtained using a reducing (e.g. Ar/H_2) thermal treatment at high temperatures (e.g. 1600 °C), whereas the higher oxidation state is formed

during oxidation at moderate temperatures (e.g. 800 °C). As the oxygen potential of such materials increases with temperature [7,31,32], oxidation at high temperatures will not favour the higher oxidation state. The oxidation state +3 is reported for Pu, Am, and Cm and, similar to their binary oxides, increases in stability from Pu to Cm. The formation of the oxidation state +4 is common for all actinides from Th to Am. Although Cm(III) is very stable [5,33], we propose that Cm(IV) can be stabilised at strongly oxidative conditions (low–moderate temperature) in a sufficient excess of oxygen vacancies. This stabilisation of the higher Cm valence should occur in analogy to Np(V) and U(VI), as the binary oxides UO_3, Np_2O_5, and CmO_2 decompose at similar temperatures [34]. An additional indication of the structural stabilisation of Cm(IV) by oxygen vacancies is the existence of $BaCmO_3$ [35], which has a much higher thermal stability than CmO_2. The oxidation state +5 is limited to Pa, U, and Np, and +6 to U only. The formation of Pa(V) should be reachable just as Pa_2O_5 is thermal stable at moderate temperatures [34]. U(V) is observed predominantly at low oxygen vacancy content in YSZ or intermediate oxygen partial pressures [13], but with increasing oxygen vacancies U(VI) becomes more stable (Fig. 2). The formation of Np(V) is strongly coupled to the presence of excess oxygen vacancies in YSZ as the oxidation process has to compete with the Zr tendency to form coordination polyhedra with less than eight oxygen atoms. For the same reason Np(VI), which is known to form fluorite-type ternary oxides with rare earths [36], is suppressed by the presence of Zr. As indicated by ^{237}Np Mössbauer spectroscopy, the lower and higher oxidation states can coexist at intermediate oxygen potential or when the oxygen vacancy concentration is limited. Because of their similar crystallography, the same actinide oxidation behaviour can be assumed for stabilised zirconia crystallising in the fluorite and pyrochlore structure. However, the feasibility to reach certain oxidation states (O/*M* ratio) might depend on the cation position on which the actinide dopant is placed in the pyrochlore structure.

Acknowledgments

We would like to acknowledge the assistance of C. Boshoven, S. Gardeur, M. Holzhäuser and P. Lajarge in the preparation of samples, Eric Colineau for Mössbauer measurements, and Ångströmquelle Karlsruhe, ANKA, for providing beamtime for the EXAFS measurements.

Appendix A. Supporting Information

Supplementary data associated with this article can be found in the online version at doi:10.1016/j.jssc.2009.09.022.

References

[1] A. Fernández, D. Haas, R.J.M. Konings, J. Somers, J. Am. Ceram. Soc. 85 (2002) 694–696.
[2] Y. Croixmarie, E. Abonneau, A. Fernández, R.J.M. Konings, F. Desmoulière, L. Donnet, J. Nucl. Mater. 320 (2003) 11–17.
[3] S.X. Wang, B.D. Begg, L.M. Wang, R.C. Ewing, W.J. Weber, K.V. Govidan Kutty, J. Mater. Res. 14 (1999) 4470–4473.
[4] G.R. Lumpkin, Elements 2 (2006) 365–372.
[5] R.G. Haire, P.E. Raison, Z. Assefa, J. Nucl. Sci. Technol. (Suppl. 3) (2002) 616–619.
[6] T. Yamashita, K. Kuramoto, M. Nakada, S. Yamazaki, T. Sato, T. Matsui, J. Nucl. Sci. Technol. (Suppl. 3) (2002) 585.
[7] H. Otobe, A. Nakamura, T. Yamashita, T. Ogawa, J. Nucl. Sci. Technol. 9 (Suppl. 3) (2002) 652.
[8] M. Walter, C. Nästren, J. Somers, R. Jardin, M.A. Denecke, B. Brendebach, J. Solid State Chem. 180 (2007) 3130–3135.
[9] C. Nästren, J. Somers, R. Jardin, B. Brendebach, M. Walter, J. Solid State Chem. 182 (2009) 1.
[10] H. Kinoshita, K. Kuramoto, M. Uno, T. Yanagi, S. Yamanaka, H. Mitamura, T. Banba, J. Am. Ceram. Soc. 83 (2000) 391–396.
[11] J.H. Handwerk, G.D. White, D.C. Hill, J. Am. Ceram. Soc. 46 (1963) 29–32.
[12] N.K. Kulkarni, S. Sampath, V. Venugopal, Ceram. Int. 27 (2001) 839–846.
[13] E.R. Vance, G.R. Lumpkin, M.L. Carter, D.J. Cassidy, C.J. Ball, R.A. Day, B.D. Begg, J. Am. Ceram. Soc. 85 (2002) 1853–1859.
[14] J.A. Fortner, A.J. Kropf, R.J. Finch, A.J. Bakel, M.C. Hash, D.B. Chamberlain, J. Nucl. Mater. 304 (2002) 56–62.
[15] C.R.A. Catlow, A.V. Chadwick, G.N. Greaves, L.M. Moroney, EXAFS study of yttria-stabilized zirconia, J. Am. Ceram. Soc. 69 (1986) 272–277.
[16] D. Komyoji, A. Yoshiasa, T. Moriga, S. Emura, F. Kanamaru, K. Koto, Solid State Ionics 50 (1992) 291–301.
[17] P. Li, I.-W. Chen, J.E. Penner-Hahn, Phys. Rev. B 48 (1993) 10074–10081.
[18] K. Kawata, H. Maekawa, T. Nemoto, T. Yamamura, Solid State Ionics 177 (2006) 1687.
[19] P. Villella, S.D. Conradson, F.J. Espinosa-Faller, S.R. Foltyn, K.E. Sickafus, J.A. Valdez, Phys. Rev. B 64 (2001) 104101.
[20] M. Walter, J. Somers, A. Fernandez, E.D. Specht, J.D. Hunn, P. Boulet, M.A. Denecke, C. Göbel, J. Mater. Sci. 42 (2007) 4650.
[21] K. Popa, E. Colineau, F. Wastin, R.J.M. Konings, J. Chem. Thermodyn. 39 (2007) 104–107.
[22] J. Rodriguez-Carvajal, FULLPROF version 3.00, ILL, Grenoble, 2004, unpublished.
[23] J. Rothe, M.A. Denecke, K. Dardenne, T. Fanghänel, Radiochim. Acta 94 (2006) 691–696.
[24] T. Ressler, J. Synchrotron Radiat. 5 (1998) 118–122.
[25] A.L. Ankudinov, B. Ravel, J.J. Rehr, S.D. Conradson, Phys. Rev. B 58 (1998) 7565–7576.
[26] S.K. Sali, N.K. Kulkarni, K. Krishnan, S.N. Achary, A.K. Tyagi, J. Solid State Chem. 181 (2008) 1859–1866.
[27] M. Yashima, S. Sasaki, M. Kakihana, Acta Cryst. B 50 (1994) 663–672.
[28] M.A. Denecke, Coord. Chem. Rev. 250 (2006) 730–754.
[29] E.A. Hudson, J.J. Rehr, J.J. Bucher, Phys. Rev. B 52 (1995) 13815–13826.
[30] C. Nästren, M. Walter, in: ANKA Annual Report 2008, ANKA Angströmquelle Karlsruhe, Forschungszentrum Karlsruhe, 2008, pp. 168–169.
[31] T.D. Chikalla, L. Eyring, J. Inorg. Nucl. Chem. 29 (1967) 2281–2293.
[32] H. Otobe, A. Nakamure, T. Yamashita, K. Minato, J. Nucl. Mater. 344 (2005) 219–222.
[33] P.E. Raison, R.G. Haire, Z. Assefa, J. Nucl. Sci. Technol. (Suppl. 3) (2002) 725–728.
[34] R.G. Haire, L. Eyring, in: K.A. Gschneidner, L. Eyring, G.R. Choppin, G.R. Lander (Eds.), Handbook on the Physiscs and Chemistry of Rare Earths, Vol. 18, Lanthanides/Actinides: ChemistryElsevier Science B. V., Amsterdam, 1994, pp. 413–505.
[35] J. Fuger, R.G. Haire, J.R. Peterson, J. Alloys Compd. 200 (1993) 181–185.
[36] C. Keller, A. Boroujerdi, J. Inorg. Nucl. Chem. 34 (1972) 1187–1193.